Supplementary Information for
Many-body delocalization with a two-dimensional 70-qubit superconducting quantum simulator

Tian-Ming Li,[1,2,*] Zheng-Hang Sun,[3,*] Yun-Hao Shi,[1,*] Zhen-Ting Bao,[1,2,*] Yong-Yi Wang,[1,2] Jia-Chi Zhang,[1,2] Yu Liu,[1,2] Cheng-Lin Deng,[4] Yi-Han Yu,[1,2] Zheng-He Liu,[1,2] Chi-Tong Chen,[5] Li Li,[1,2] Hao Li,[4] Hao-Tian Liu,[1,2,4] Si-Yun Zhou,[1,2] Zhen-Yu Peng,[1,2] Yan-Jun Liu,[1,2] Ziting Wang,[4] Yueshan Xu,[4] Kui Zhao,[4] Yang He,[1,2] Da'er Feng,[1,2] Jia-Cheng Song,[1,2] Cai-Ping Fang,[1,2,4] Junrui Deng,[1,2] Mingyu Xu,[1,2] Yu-Tao Chen,[1,2] Bozhen Zhou,[6] Gui-Han Liang,[1,2] Zhongcheng Xiang,[1,2] Guangming Xue,[4] Dongning Zheng,[1,2] Kaixuan Huang,[4] Zheng-An Wang,[4] Haifeng Yu,[4,†] Piotr Sierant,[7] Kai Xu,[1,2,4,8,9,‡] and Heng Fan[1,2,4,8,9,§]

[1]*Beijing National Laboratory for Condensed Matter Physics, Institute of Physics, Chinese Academy of Sciences, Beijing 100190, China*
[2]*School of Physical Sciences, University of Chinese Academy of Sciences, Beijing 100049, China*
[3]*Theoretical Physics III, Center for Electronic Correlations and Magnetism, Institute of Physics, University of Augsburg, D-86135 Augsburg, Germany*
[4]*Beijing Key Laboratory of Fault-Tolerant Quantum Computing, Beijing Academy of Quantum Information Sciences, Beijing 100193, China*
[5]*Quantum Science Center of Guangdong-Hong Kong-Macao Greater Bay Area, Shenzhen, Guangdong 518045, China*
[6]*Institute of Theoretical Physics, Chinese Academy of Sciences, Beijing 100190, China*
[7]*Barcelona Supercomputing Center, Barcelona 08034, Spain*
[8]*Hefei National Laboratory, Hefei 230088, China*
[9]*Songshan Lake Materials Laboratory, Dongguan, Guangdong 523808, China*

CONTENTS

* These authors contributed equally to this work.
† hfyu@baqis.ac.cn
‡ kaixu@iphy.ac.cn
§ hfan@iphy.ac.cn

Section 1. EXPERIMENTAL SETUP AND DEVICE PERFORMANCE

A. Experimental setup

A cryogenic environment of ∼10 mK was realized and maintained using a Bluefors XLD-1000 dilution refrigerator to minimize thermal excitation for controlling superconducting circuits. As shown in Fig.S1, carefully selected attenuators and filters are arranged along the signal lines between room temperature (RT, ∼300 K) and the extremely low base temperature, effectively suppressing thermal noise and thereby protecting the quantum circuits (qubits and couplers).

High-frequency XY pulses (∼ 4 GHz) and readout pulses (∼ 7 GHz) are generated using in-phase/quadrature (IQ) modulation [1]. This technique combines the dual-channel arbitrary waveforms (frequencies below 500 MHz) generated by digital-to-analog converter (DAC) with microwave source (fixed at 3.350 GHz, 4.350 GHz, 6.675 GHz, 7.425 GHz in our experiment, respectively) produced by a local oscillator (LO). The intrinsic leakage from the LO signal is suppressed to approximately -90 dBm through zero calibration. The Z control for both qubits and couplers were generated by the similar DAC, which operating at 2 Gs/s with 16-bit vertical resolution. For couplers, the Z control signal is directly sent into the processor through coaxial cables and microwave components. In contrast, for qubits, the Z control signal is combined with the excitation pulse (XY signal) through a directional coupler prior to transmission. The joint readout signals are sent through the transmission line, sequentially amplified by a high electron mobility transistor (HEMT) and a room temperature RF amplifier (RFA), and finally demodulated by a dual-channel analog-digital converter (ADC) operating at 1 Gs/s with 14-bit vertical resolution. All electronic devices are synchronized via a clock-and-trigger generator paired with distributors. The generator is fed by a 10 MHz reference originated from the rubidium atomic clock, while the distributors up-convert this 10 MHz signal to 250 MHz and then disseminate it throughout the system. These distributors also route trigger signals to all DACs and ADCs.

B. Device architecture

We conduct the experiments on a 72-qubit superconducting quantum processor arranged in 2D rectangular array (shown in Fig.S2(a)) similar to Sycamore [2], including 12 readout lines, each coupled to 6 qubits. Each qubit is tunably coupled to its four nearest-neighbors (NN) typically, resulting in 121 tunable couplers used to flexibly control the effective coupling strength between qubits pairs.

In our experiments, only 70 qubits and 117 couplers on the processor are utilized. Qubit Q_{65} is discarded due to its strong coupling with an external two-level system (TLS), which also results in the exclusion of Q_{71}, as it becomes effectively isolated. As shown in Fig.S2(b), the spectroscopy of Q_{65} reveals a pronounced avoided crossing (anti-crossing), indicating the presence of a TLS at approximately 3.9 GHz with a coupling strength of about 50 MHz to Q_{65}. Fig.S2(c) further demonstrates the unwanted coherent exchange between Q_{65} and the TLS, which adversely affects the experiment. Four couplers which connect to either Q_{65} or Q_{71} are therefore excluded from consideration.

C. Device performance

In summarize, Fig.S3 and Fig.S4 list the basic performance of the qubits, including:

- Qubit frequency, including $|0\rangle$ to $|1\rangle$ transition frequency at the idle point $f_{10}^{\rm idle} = \omega_{10}^{\rm idle}/2\pi$.
- Qubit sweet point (maximum) transition frequency $f_{10}^{\rm sw} = f_{10}^{\rm max} = \omega_{10}^{\rm max}/2\pi$.
- Qubit anharmonicity $\eta/2\pi = f_{21} - f_{10} < 0$, where f_{21} is $|1\rangle$ to $|2\rangle$ transition frequency.
- Energy relaxation time at idle point $T_1^{\rm idle}$.
- Average energy relaxation time in the vicinity of resonant working point $T_1^{\rm WP}$ (range of 3.520 ± 0.100 GHz).
- Dephasing time, including Ramsey dephasing T_2^* and spin-echo dephasing $T_2^{\rm SE}$ at the idle point.
- Readout resonator frequency f_r.
- Single-qubit gate error rates for I and X gates measured using quantum state tomography (QST).

The detailed average performances of these parameters are displayed using vertical and horizontal lines shown in Fig.S4. We emphasize that the average energy relaxation time of both idle points and resonant working points are above 50 μs.

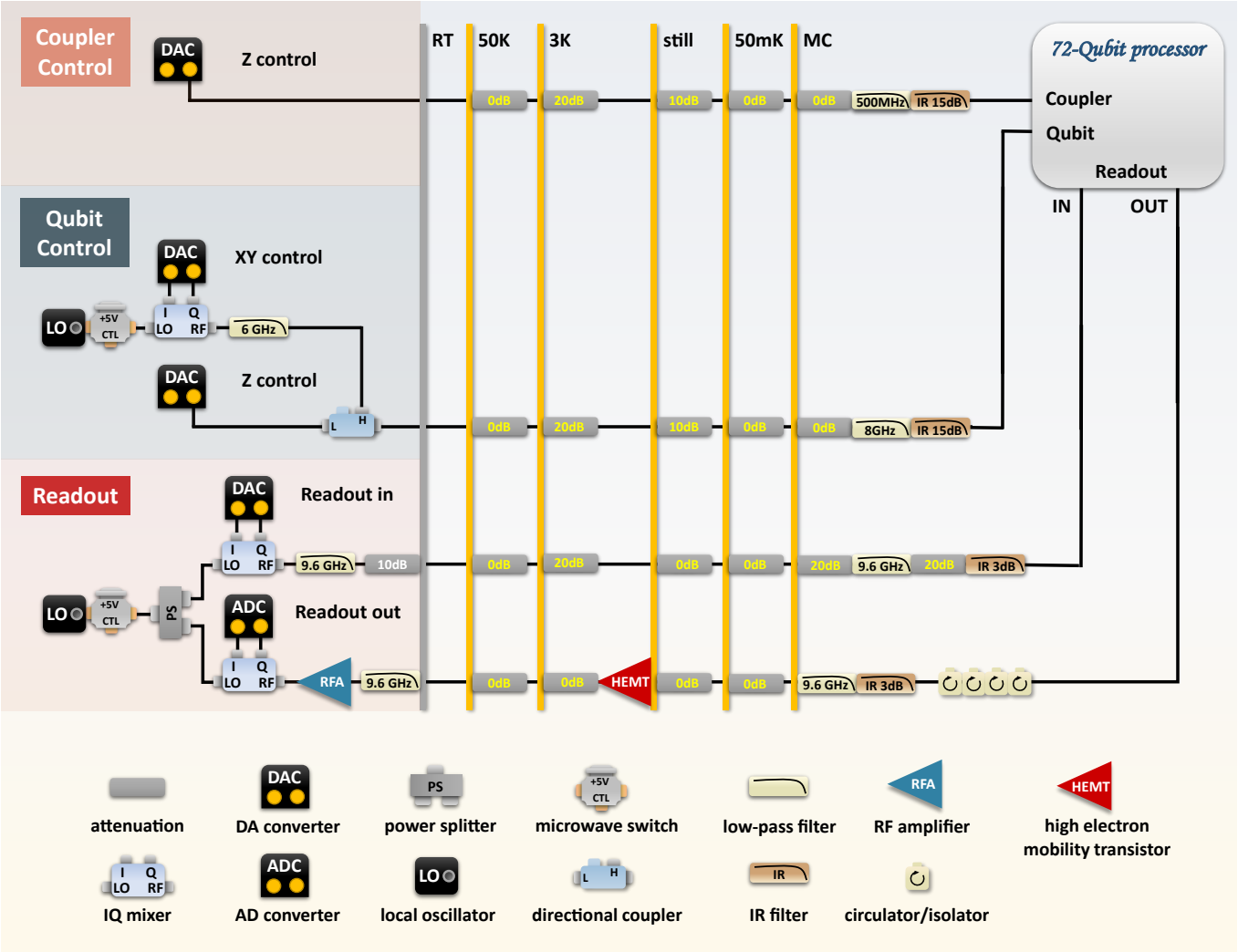

FIG. S1. **Schematic diagram of electronic devices and wiring information.**

D. Effective coupling strength

To realize tunable interactions between qubits, we adopt the QubitCouplerQubit (QCQ) architecture [3]. In this architecture, two NN qubits with frequencies ω_1 and ω_2, coupled directly with strength g_{12}, are principally coupled to an intermediate tunable coupler with frequency ω_c, with coupling strengths g_{1c} and g_{2c}, respectively. The effective coupling strength is then given by [4]

$$g_{\text{eff}} = g_{12} + \frac{g_{1c}g_{2c}}{2}\left(\frac{1}{\omega_1 - \omega_c} + \frac{1}{\omega_2 - \omega_c}\right), \tag{S1}$$

which can be adjusted by applying a suitable Z pulse amplitude to the coupler to modulate its frequency ω_c. Fig.S5(a) shows the typical experimental dependence of the effective coupling strength g_{eff} as a function of the coupler Z pulse amplitude.

In our experiments, we characterize the effective coupling strengths between all NN qubit pairs [Fig.S6(a), typical data in Fig.S5(b)], as well as next-nearest-neighbour (NNN) qubit pairs in horizontal direction [Fig.S6(b), typical data in Fig.S5(c)], where the resonance point is set at 3.520 GHz. Due to the asymmetric floating layout of the coupler [5], horizontal qubit pairs are placed physically closer than vertical pairs. As a result, the coupling strengths are significantly different: horizontal pairs exhibit a typical strength around 1 MHz, while vertical pairs are weakly coupled by strength around 0.1 MHz and can be considered effectively decoupled.

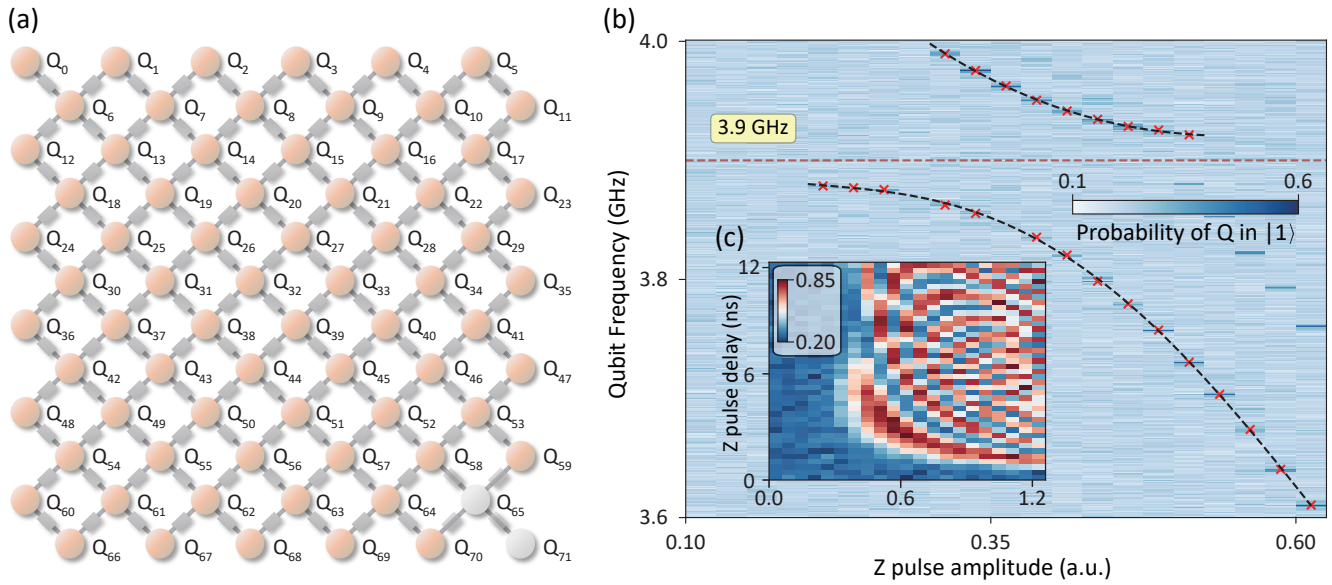

FIG. S2. **Schematic of chip layout and characterizations of TLS strongly coupled to qubit Q_{65}.** (a) Layout of the quantum chip comprising a 2D array of 72 superconducting qubits and 121 couplers. Circles represent qubits, while rectangles represent couplers. Qubit Q_{71} and 4 couplers (colored lighter gray) connected to Q_{65} were not used in the experiments. Qubit labels follow a numbering sequence based on their physical locations. (b) Qubit spectroscopy of Q_{65}, showing a pronounced anti-crossing at approximately 3.9 GHz, indicative of strong coupling to a two-level system (TLS). The black dashed lines are fits to the upper and lower hybridized branches, while the red dashed line marks the TLS transition frequency. (c) Spectrally resolved T_1 of Q_{65} in $|0\rangle$ after excitation, shown as the function of Z pulse amplitude. The persistent oscillations indicate coherent exchange between the qubit and the TLS.

Section 2. DEVICE CONTROL AND CALIBRATION

Controlling superconducting quantum processor with 70 qubits and 117 couplers is a highly complex task, posing some significant challenges in achieving a well-calibrated operational state across all qubits and couplers. This is crucial for accurately simulating dynamics related to system imbalances. Therefore, an automated and standardized calibration procedure is essential to ensure high-precision and stable control throughout the entire chip. In particular, when simulating the targeted many-body Hamiltonian, control parameters, such as flux bias used to tune qubits from their idle points to specific resonant working points, are required to be carefully optimized and validated.

In this section, we outline the experimental details into two main parts: (i) *automation technique*, which facilitates the initialization of our device on both the single-qubit and multi-qubit levels, and (ii) *precision calibration*, which enables the accurate simulation for quantum many-body systems.

A. Automation technique for scalable processor

1. *Automatic qubit bringing-up*

Following a round of initial calibration across the entire processor, we obtain some basic information, typical data of which is displayed in Fig.S7:

- Qubit spectroscopy, which establishes the relationship between flux bias and transition frequency.
- The response of the readout signal amplitude as a function of drive frequency and amplitude [6, 7], which determines the appropriate readout power for each qubit.
- Flux signal correction [8, 9], achieved by predistorting Z pulse using the step response function measured at a calibration working point approximately 0.8 GHz below the sweet point, thereby providing enhanced resolution due to the increased sensitivity of the flux bias.
- Qubit spectrally resolved T_1 (i.e., spectrum of T_1), which detects defects arising from existing TLSs.
- Classical flux crosstalk between nearest-neighbour (NN, such as qubit and nearby coupler) and next-nearest-neighbour (NNN, such as qubit pairs) circuits is originally maintained below 0.1%.

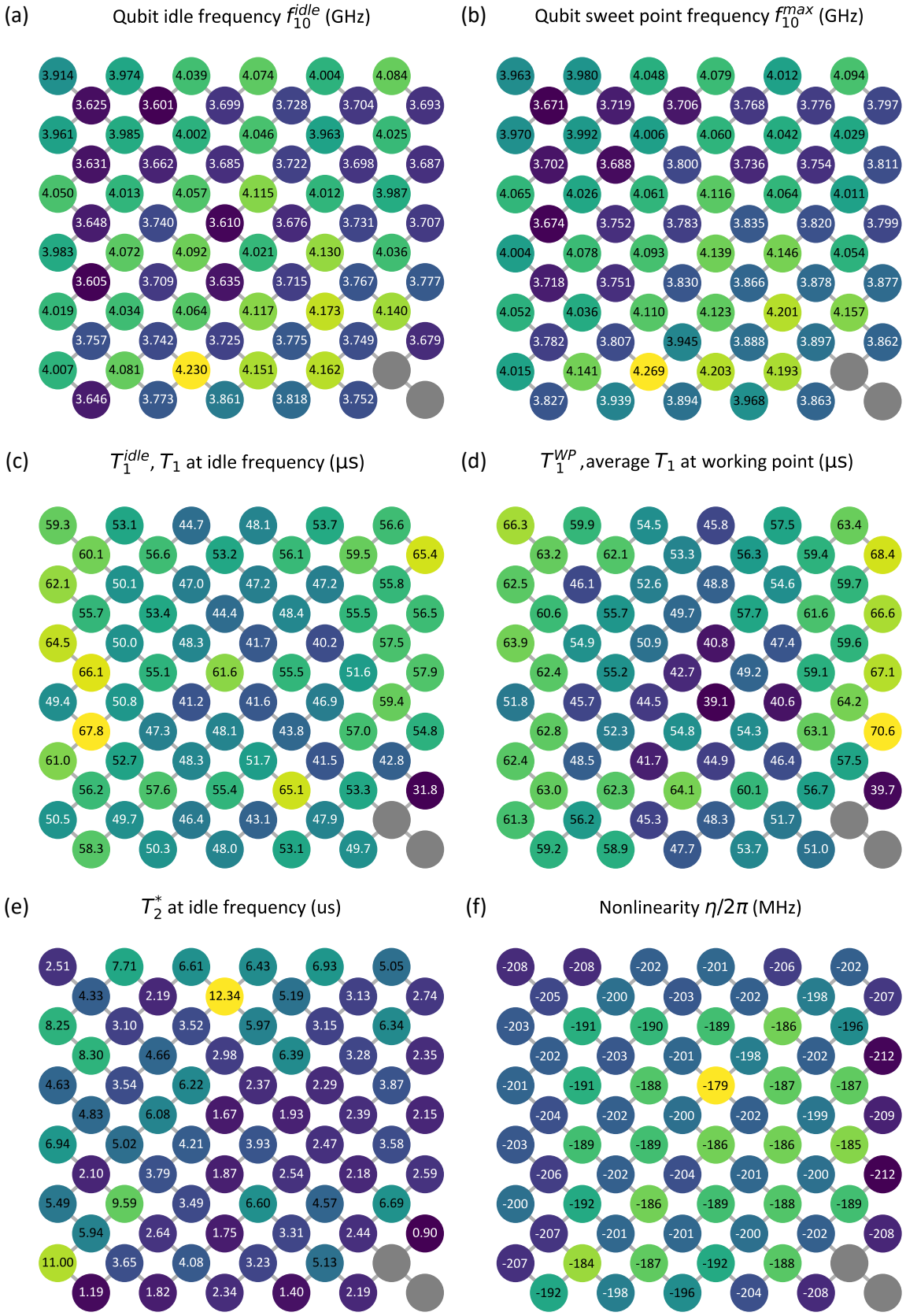

FIG. S3. **Distribution of single-qubit performance parameters across the processor.** (a) Qubit $|0\rangle$ to $|1\rangle$ transition frequency at idle point, f_{10}^{idle}. (b) Sweet point (maximum transition) frequency, f_{10}^{max}. (c) Energy relaxation time at idle point, T_1^{idle} and (d) average energy relaxation time near resonant working point T_1^{WP}. (e) Ramsey dephasing time, T_2^* at idle point. (f) Qubit anharmonicity, $\eta/2\pi$. In all panels, black entries indicate values above the mean, while white entries denote values below the mean.

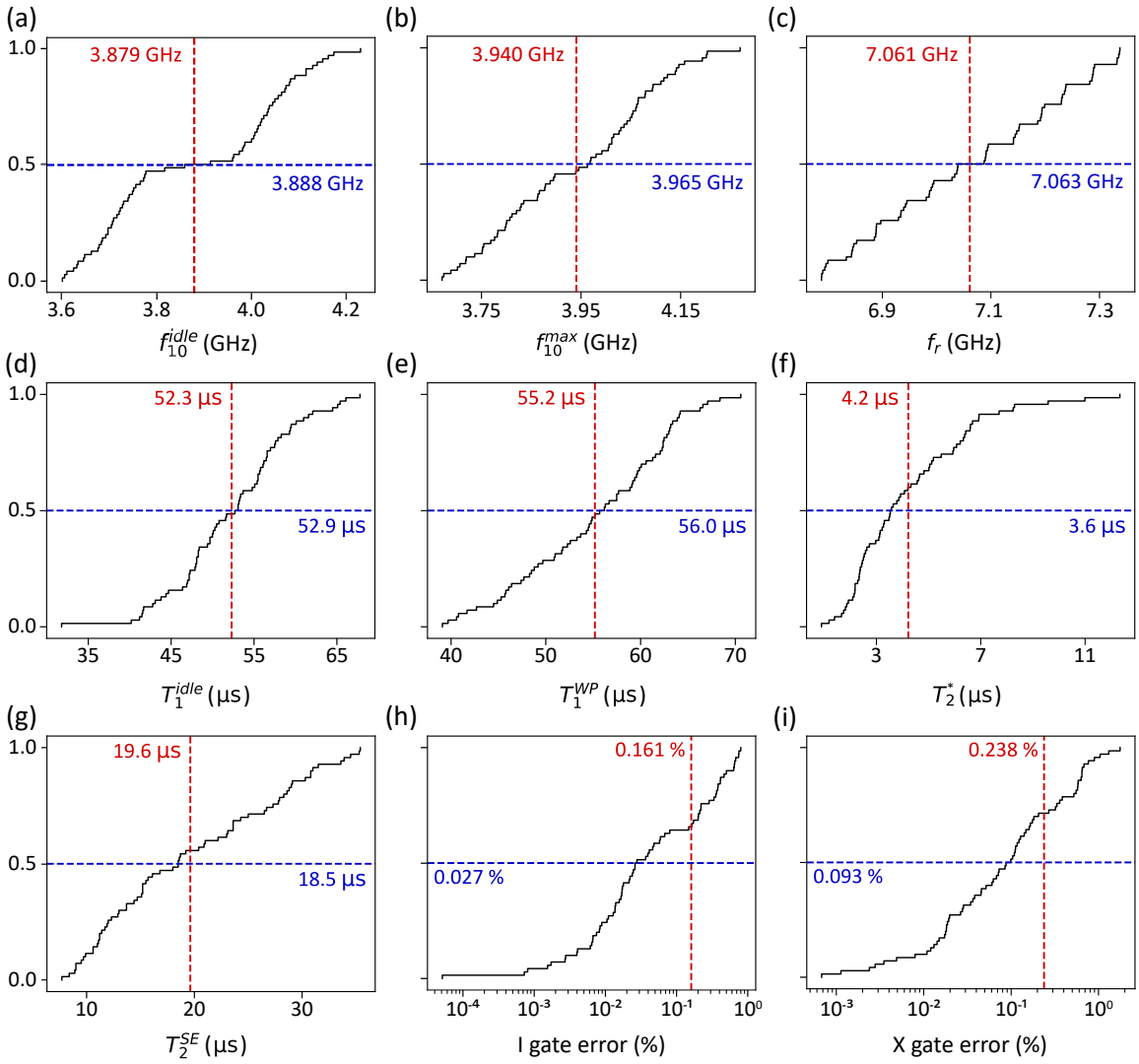

FIG. S4. **Integrated histrogram of chip performance.** (a) Qubit $|0\rangle$ to $|1\rangle$ transition frequency at idle point, f_{10}^{idle}. (b) Sweet point (maximum transition) frequency, f_{10}^{max}. (c) Readout frequency, f_r. (d) Energy relaxation time at idle point, T_1^{idle}, and (e) average energy relaxation time near resonant working point, T_1^{WP}. (f) Ramsey dephasing time, T_2^*, and (g) spin-echo dephasing time, T_2^{SE}, at idle point. Single-qubit (h) I gate error rate and (i) X gate error rate. Red vertical lines indicate mean values, while blue horizontal lines denote median values.

The qubit spectroscopy serves as the foundation for the subsequent automated qubit bring-up process, ensuring that each qubit is initialized at its expected frequency. This procedure consists of several sequential steps, as outlined in flowchart in Fig.S7:

- Set the flux bias of each qubit based on its spectroscopy to bring the qubit close to its desired idle frequency.
- Establish a suitable readout power determined from the response function referred.
- Configure the readout frequency to match the frequency of readout resonator when qubit is in state $|0\rangle$.
- Perform power Rabi oscillations to obtain an initial estimate of the 30 ns π pulse amplitude.
- Fine-tune the qubit bias to the target value using Ramsey experiments, minimizing detuning errors in single-qubit gates.
- Recalculate the gate parameters (amplitudes) to renormalize the single-qubit gate duration into 120 ns, which reduces the frequency bandwidth of excitation pulse, thereby mitigating errors caused by classical XY crosstalk.
- Apply DRAG [10] correction (including optimizing DRAG coefficient and fine-tuning gate amplitude) to mitigate leakage out of computational subspace and control errors, thus realizing high-fidelity single-qubit gates.
- Optimize the readout frequency by characterizing the dispersive shift, achieving higher readout visibility and fidelity.
- Perform calibration for IQ readout signals to discriminate between states $|0\rangle$ and $|1\rangle$ before any probability-based readout experiment, ensuring accurate state classification.

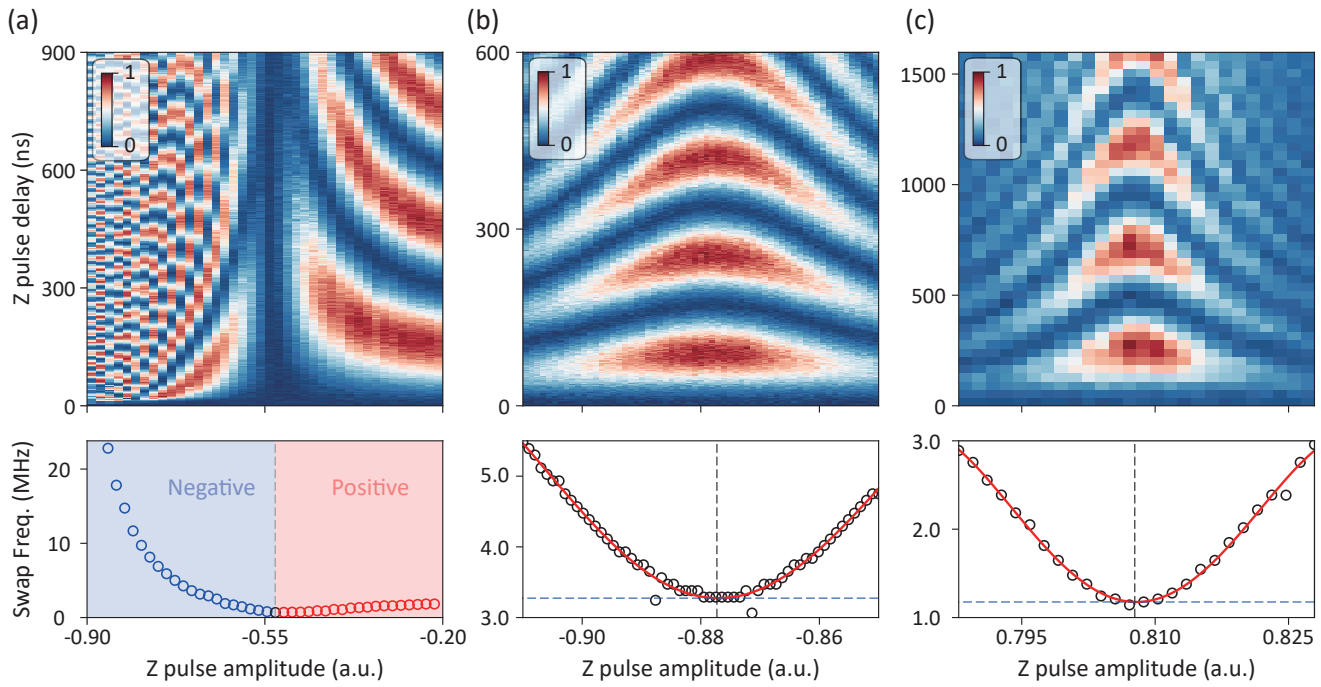

FIG. S5. **Modulation and accurate measurement of effective coupling strength using two-qubit swap spectroscopy.** The top row shows the time-dependent probability of the qubit pair occupying $|01\rangle$ after initialization in $|10\rangle$, while the bottom row displays the corresponding swap frequencies obtained via Fourier transform. (a) Two NN qubits are both biased at 3.520 GHz, while the tunable coupler bias is varied via scanned Z pulse amplitude. In lower panel, the shaded red and blue regions denote positive and negative effective coupling strengths, respectively. Precise measurement of effective coupling strength for (b) an NN qubit pair and (c) a horizontally adjacent NNN qubit pair. One qubit remains fixed at 3.520 GHz, the other one is swept through resonance, while the coupler bias holds constant for fixing coupling strength. The effective coupling strength is extracted by fitting the minimum swap frequency observed in the Fourier transformed spectra.

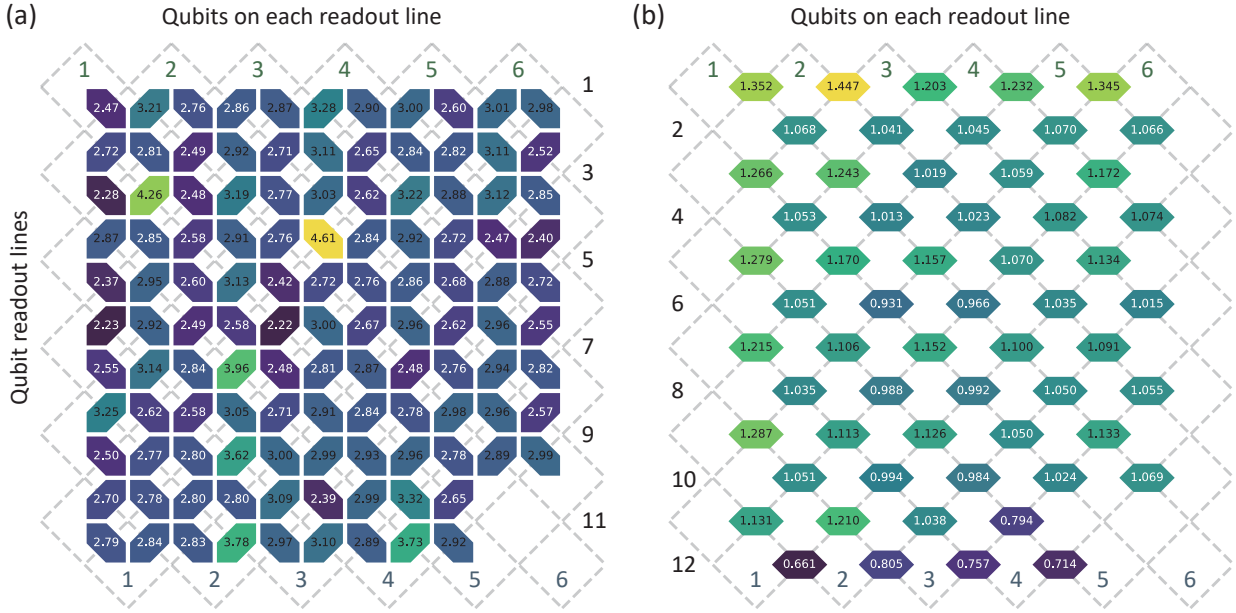

FIG. S6. **Effective coupling strengths.** Effective coupling strengths (in MHz) are shown for (a) NN qubits and (b) horizontally adjacent qubits. In each panel, black entries denote values above the mean coupling strength, while white entries denote values below the mean.

Automated bring-up of individual qubits forms a crucial foundation for the subsequent calibration processes, such as multi-qubit energy level arrangement. This approach provides an efficient, black-box technique that enhances the overall integration of automation in our system.

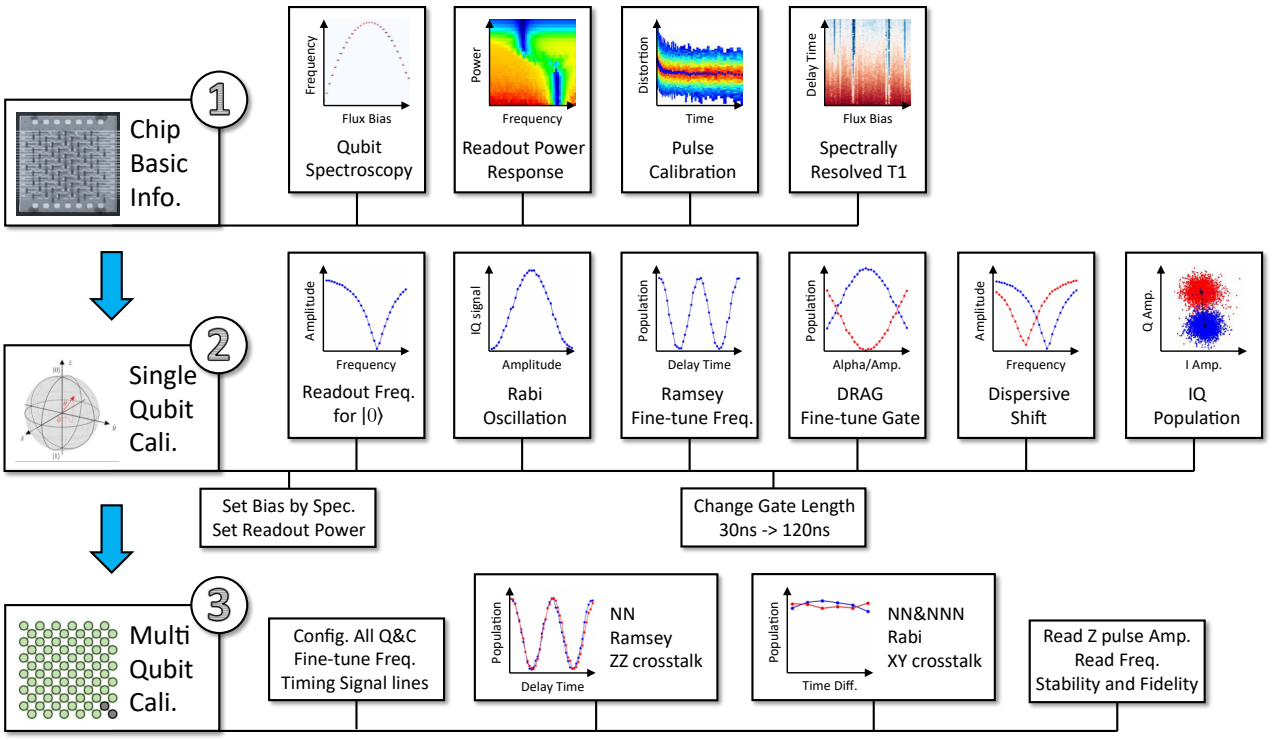

FIG. S7. **Flowchart and representative data for automation techniques.** Part 1: Basic characterization of the chip, including (from left to right) qubit spectroscopy, readout signal amplitude as a function of drive frequency and power, flux pulse distortion and correction, and qubit spectrally resolved T_1. Part 2: Automated single-qubit bring-up. Sequential calibration steps are shown, along with corresponding representative data (see Section 2 A 1 for details). Part 3: Multi-qubit calibration. Workflow diagram illustrating how automated procedures establish a stable idle configuration with high-fidelity, stable readout and suppressed crosstalk (details in Section 2 A 2).

2. *Automatic allocation of qubit idle points*

Based on the fundamental information (particularly qubit spectroscopy and spectrally resolved T_1) obtained in Section 2 A 1, we establish a series of constraints for configuring the idle energy levels of qubits:

- The idle frequency should not be set too close to or too far from the qubit sweet point. If the idle frequency is placed too near its sweet point, achieving this non-realistic target frequency might fail due to fitting errors in qubit spectroscopy. Conversely, setting idle point too far away could lead to short dephasing time (T_2^*). In our experiments, the idle frequency is restricted to be within 1 MHz to 250 MHz below the sweet point of the aiming qubit, as indicated between the dashed lines in Fig.S8(a).

$$f^{\mathrm{sw}} - 250\ \mathrm{MHz} < f^{\mathrm{idle}} < f^{\mathrm{sw}} - 1\ \mathrm{MHz} \tag{S2}$$

- Regions where qubits exhibit short coherence time (T_1) due to existing TLSs are identified and avoided, utilizing the measured spectrally resolved T_1, as shown in Fig.S8(b).

$$f^{\mathrm{idle}} \notin \{f : f_{\mathrm{TLS}}\} \tag{S3}$$

- The detuning Δ between NN and NNN qubits, should be significantly stronger than the stray coupling g between them. For our devices, as illustrated in Fig.S8(c), we consider directly coupled NN, two types of diagonal NNN (vertical and horizontal), and NNN connected through an intermediate qubit. The corresponding coupling strengths are approximately

4 MHz, 0.1 MHz, 1 MHz, and 0.2 MHz, respectively. Therefore accordingly, the required detunings are restricted to be greater than 250MHz (accounting for anharmonicity of transmon is around 200 MHz), 2 MHz, 10 MHz, and 5 MHz, respectively. Additionally, the detuning between any two qubits is also constrained to be at least 2MHz to avoid classical XY crosstalk.

$$\Delta \gg g,\ \Delta_{\text{idle}} > \Delta_{\text{set}} \tag{S4}$$

This constraint optimization problem is answered by the Satisfiability Modulo Theory (SMT) solver implemented with the Python "pysmt" package [11]. With the resulting energy level allocation, the automated qubit bring-up black-box described in Section 2 A 1 is then applied to achieve the preparation for multi-qubit idle configuration.

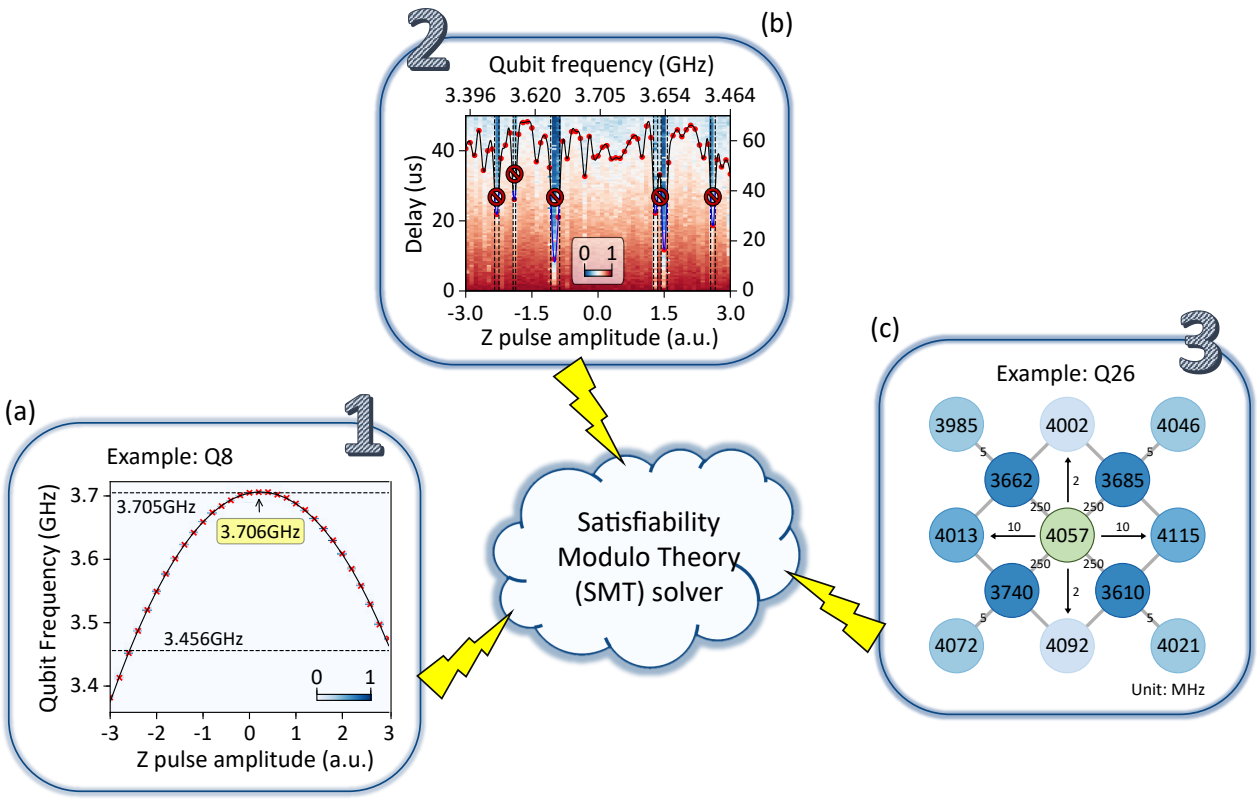

FIG. S8. **Schematic of constraints for automated energy levels allocation.** (a) Constraint 1: The idle point should be neither too close nor too far from the sweet point. For example, as shown in the qubit spectroscopy of Q_8, an acceptable idle frequency window (1250 MHz below the sweet point) is indicated between the two black dashed lines. (b) Constraint 2: Frequencies with poor coherence must be avoided. As shown in spectrally resolved T_1 for Q_8, the region between the black dashed lines corresponds to qubit frequencies where T_1 falls below an acceptable threshold. For 2D heat map, delay follows the left y-axis. While the red dots represent the fitted T_1 for experiment points, delay of which follows the right y-axis. The black-blue curve means the fitted T_1 as a function of qubit bias, where black indicates $T_1 > 40$ μs and blue indicates $T_1 < 40$ μs. (c) Constraint 3: Detuning Δ must be much greater than the coupling strength g. A schematic of the energy level configuration around Q_{26} (green) is shown. Neighboring qubits are detuned by at least 250 MHz, 10 MHz, 5 MHz, and 2 MHz, which are annotated on the links. The qubit circles are filled with color from dark blue to light blue, according to their effective coupling strength.

After initializing each qubit according to the SMT-optimized energy levels allocation, we configure all qubits together and perform the following series of checks and optimizations for the multi-qubit system, flowchart of which is shown in :

- Fine-tune qubit flux bias using Ramsey experiments, as residual classical Z crosstalk from other qubits is still present.
- Synchronize all control pulses (XY and Z signals), including those for qubits and couplers, using the automated technique described in the following Section 2 A 3.
- For NN qubit pairs, check the ZZ coupling strength by measuring the frequency shift (via Ramsey experiments) of one qubit (target) when the other (control) is excited. Adjusting idle frequency of the coupler between the qubits can reduce this quantum ZZ crosstalk to below 0.1 MHz.

- For NN qubit pairs, check the XY coupling strength by comparing the simultaneous excitation probabilities of the target qubit when the control qubit is either excited or not. Tuning the readout frequency of the coupler between the qubits can reduce the quantum XY crosstalk to within 1%.
- For NNN qubit pairs, check the XY coupling strength and determine whether the observed XY crosstalk originates from simultaneous excitation or readout. This is achieved by re-exciting (i.e., reset) the control qubit to its ground state before simultaneous readout. If the crosstalk disappears after reset, it can be then attributed to readout and can be suppressed by adjusting the qubits readout frequencies. Otherwise, this crosstalk is then induced by excitation and can only be mitigated by adjusting the qubits idle frequencies.
- For qubit pairs with close-frequency readout resonators (primarily, vertical diagonal NNN pairs), the readout frequencies should be separated as much as possible to reduce classical crosstalk during simultaneous readout. Typically, the qubit readout frequency is required to far bias from its sweet point to achieve this separation.
- Evaluate the stability of readout fidelity for all qubits. Re-adjust the readout frequency if necessary.

Thus far, a multi-qubit idle configuration with stable readout and well-suppressed crosstalk is finally achieved. This forms a solid foundation for the subsequent calibration for simulating quantum many-body systems.

3. *Automatic synchronization of control pulses*

Differences in the lengths of the transmission lines used for distributing trigger signals to various electronic devices, as well as slight timing variations in the control signals transmitted through coaxial cables and microwave components, necessitate the synchronization of all control pulses. We provide an automated timing procedure (pseudo-code see Algorithm 1) which consists of the following steps:

- [Fig.S9(c)] Align XY and Z signals for each individual qubit (named as "single-qubit timing calibration").
- [Fig.S9(a)] Construct breadth-first search (BFS) [11] based on the chip topology, starting from its center. This algorithm not only enables rapid conduction of the synchronized timing but also generates detailed spatial coordinates for the chip structure, which can be used to create, for instance, quasi-periodic disorder patterns.
- [Fig.S9(d)] Align the timing between qubits pairs using qubit-qubit swapping experiment (named as "QQswap") [12].
- [Fig.S9(e)] Iterate over all couplers. Based on the above qubit-qubit swapping, adjust the coupler flux bias to effectively decouple the qubits (named as "QQswap_C"), thereby aligning the coupler Z signal with its nearby qubit.

The pulse sequences and typical data are illustrated in Fig.S9. In the single-qubit timing calibration experiment, the qubit is biased away from its idle point. When the XY and Z signal timing is correctly aligned, the qubit fails to excite, producing a pronounced dip in its population, as shown in Fig.S9(c). Furthermore, we detail the QQswap and QQswap_C protocols, both of which begin by identifying a bias point that yields fully coherent exchange. The waveform schematic is given in Fig.S9(b). Initially, the bias of one qubit is finely adjusted so that its resonance (3.520 GHz in our setup) matches that of its partner, as shown in Fig.S9(d1). Next, the exchange period T for the above resonant bias is calibrated, as depicted in Fig.S9(d2). A swapping time of $t_{\mathrm{swap}} \approx T/4$ is chosen as the criterion. By shifting the bias of one qubit, maximum swapping (manifested as a peak in the population of the initially unexcited qubit) occurs only when the two Z signals are synchronized (see Fig.S9(d3)). Following the similar exchanging working point, a coupler bias is introduced and scanned to effectively decouple the qubit pair. When the coupler Z signal is synchronized with both qubits, the swapping is then maximally suppressed, resulting in a deep minimum in the population of the unexcited qubit (Fig.S9(e)). Following these steps, we can establish the precise timing alignment for both qubit and coupler control lines.

Algorithm 1: Automatically synchronize control pulses

Data: starting qubit Q, chip topology G
Result: synchronized control pulses, including qubit XY and Z signals, and coupler Z signals

qubits pairs $P_s(Q_a, Q_b) \leftarrow$ BFS for G starting from Q, couplers $C_s \leftarrow G$;
Aligned XY and Z signal for $Q \leftarrow$ Single-qubit timing calibration for Q;
for $(Q_a, Q_b) \in P_s(Q_a, Q_b)$ **do**
    Aligned XY and Z signal for $Q_b \leftarrow$ Single-qubit timing calibration for Q_b;
    Timing between qubit pair (Q_a, Q_b), update XY and Z signal timing for $Q_b \leftarrow$ QQswap for (Q_a, Q_b);
end
for $C \in C_s$ **do**
    $(Q_a, Q_b) \leftarrow$ locate C in G;
    Update Z signal timing for $C \leftarrow$ QQswap_C for (Q_a, Q_b);
end

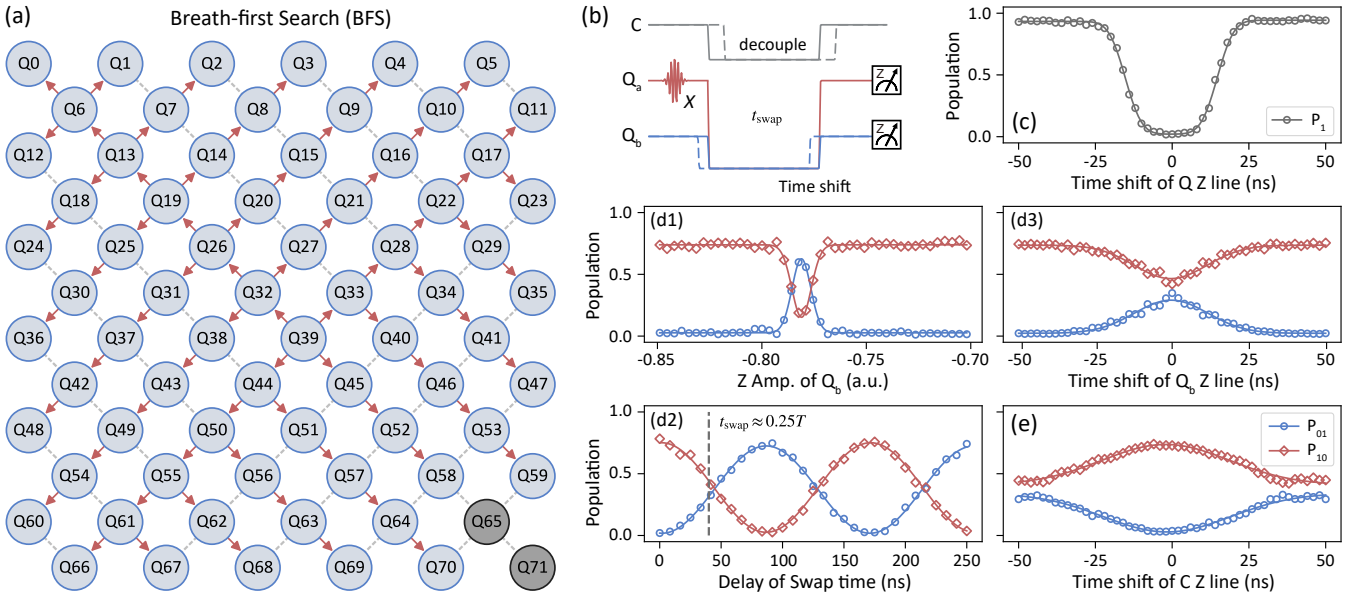

FIG. S9. **Schematic and typical data for automated pulse synchronization.** (a) Schematic of the breadth-first search (BFS) algorithm starting from qubit Q_{39}. Red arrows indicate the propagation path, where each newly aligned qubit serves as the reference for the next ones. (b) Pulse sequences used in (d) QQswap and (e) QQswap_C experiments. (c) Typical data for single-qubit timing calibration experiment, demonstrating synchronization of the XY and Z control lines for an individual qubit. (d) Typical data for QQswap experiment: (d1) identifying the bias point for fully coherent exchange, (d2) calibrating the exchange period T, and (d3) aligning the qubit pair by observing the population peak at $t_{\mathrm{swap}} \approx T/4$. (e) Typical data for QQswap_C experiment, which synchronize Z signal of the coupler with its neighboring qubits, evidenced by maximal suppression of the swap oscillation.

B. Precise calibration for aiming Hamiltonian

Given the well-prepared multi-qubit configuration, we process with simulating the quantum many-body Hamiltonian after performing targeted calibrations. In this section, the calibration process is divided into two main parts: (i) *calibrating bias for resonance*, which measures the specific resonant frequency using time-domain Rabi oscillations and then scans a fine spectrum of qubit transition within approximately $\pm$100 MHz around this resonant working point, and (ii) *checking control bias for all circuits*, which delivers multi-qubit on-resonant experiments on different block segments (derived from 70 qubits, shown in Fig.S10) to verify the control parameters, including bias for qubits to its resonant working point and bias for couplers to ideal effective coupling strength, are as expected.

1. *Calibrate specific resonant frequency using time-domain Rabi oscillation*

Due to residue Z crosstalk and parasitic couplings, the qubit frequency may slightly deviate from its expected bare frequency when all the qubits are simultaneously biased and thus dressed [13]. To address this issue, we introduce a calibration method that precisely determines the resonant frequency by measuring parameters under similar simultaneous biasing conditions.

As illustrated in Fig.S11(b), we define two configurations for calibrating the target qubit frequency. In both cases, the NN, NNN, and remaining qubits are detuned by $\pm\Delta_{\mathrm{NN}}$, $\pm\Delta_{\mathrm{NNN}}$, and $\pm\Delta_{\mathrm{rest}}$, respectively, from the target frequency. In the first configuration (named as "UP" mode), all surrounding qubits are biased above the target frequency, whereas in the second configuration (named as "DOWN" mode), they are biased below. We then perform time-domain Rabi oscillations under both configurations, as shown in Fig.S11(a), and determine the precise Z pulse amplitude Z_{target} which brings the target qubit into resonance. This value is obtained by averaging the Z pulse amplitudes from both configurations, effectively mitigating calibration errors introduced by the interaction-induced shifts [12].

To further enable precise control over on-site potentials (i.e., disorders), we perform the detailed qubit spectroscopy within the vicinity of the target frequency, covering the range corresponding to the maximum disorder strength (see typical data in Fig.S11(c)). Arbitrary on-site potentials are then realized by appropriately adjusting the Z pulse amplitude. Specifically, the required amplitude is calculated by adding the difference of the Z amplitudes between the desired disordered frequency and the resonance frequency using detailed spectroscopy to the calibrated Z_{target} obtained from Rabi oscillations.

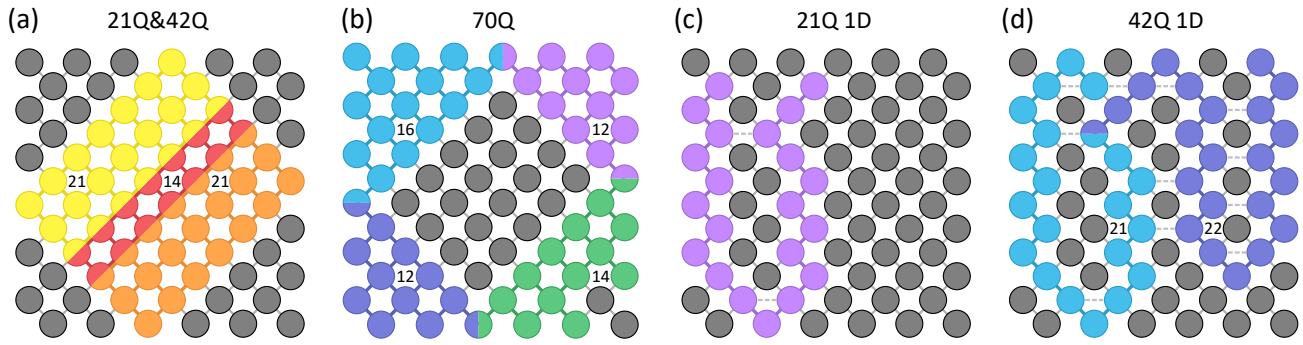

FIG. S10. **Detailed block segmentation for different system sizes.** (a) Two distinct 21-qubit systems (yellow and orange) are shown, along with a two-dimensional 42-qubit system composed by combining these two blocks with an additional sandwiched 14-qubit block (red) serving as the connection. (b) Segmentation of a 70-qubit system. The central 42-qubit block (segmented identically to (a)) is surrounded by four corner subsystems containing 12, 12, 14, and 16 qubits (colored dark blue, purple, green, and light blue, respectively). (c) A one-dimensional (1D) 21-qubit chain system (purple). (d) A 42-qubit 1D chain divided into 21-qubit and 22-qubit subsystems (light blue and dark blue, respectively). The dashed gray lines in (c-d) represents the NNN couplings J_{ij}^{NNN}, which slightly non-idealize the 1D chains.

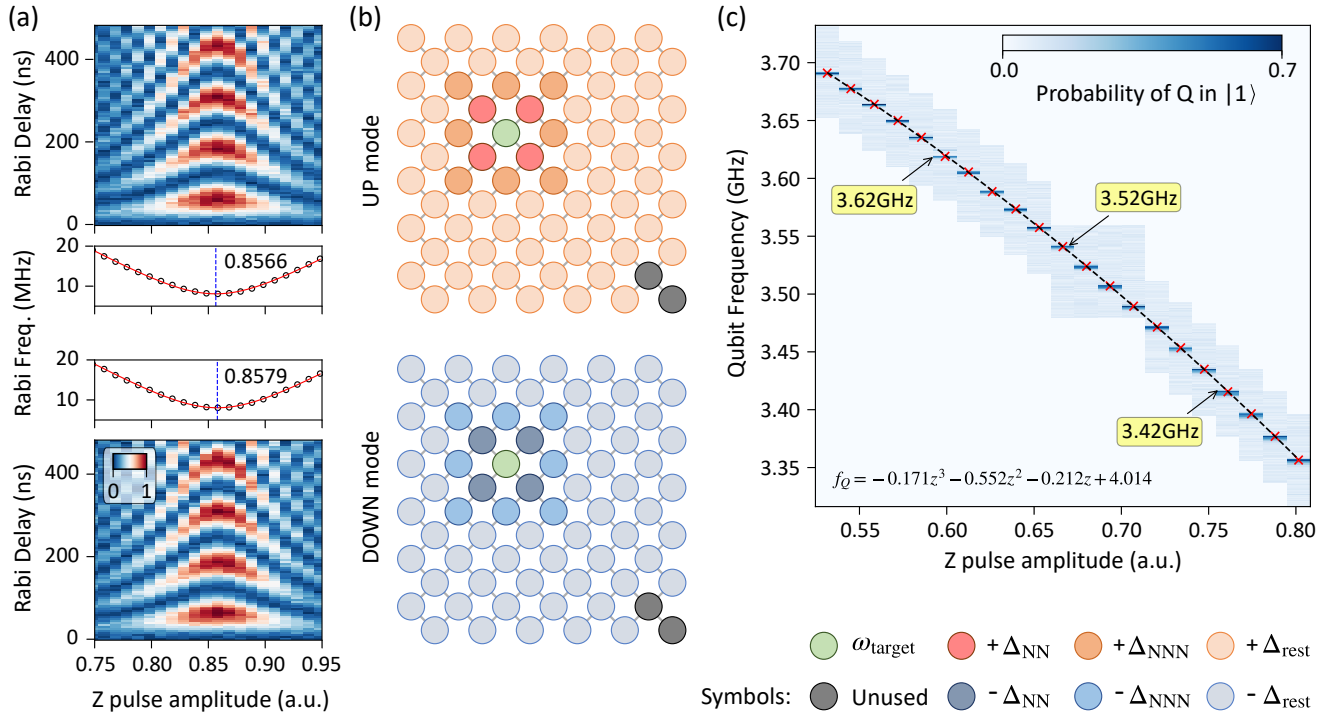

FIG. S11. **Typical experimental data and configurations for calibrating on-site potentials.** (a) Time-domain Rabi oscillations measured in both UP and DOWN biasing modes. The heatmap represents the probability of qubit in $|1\rangle$. The Fourier transformation of this data shows the Rabi frequency as a function of the Z pulse amplitude. The precise Z pulse amplitude Z_{target} is determined as the mean amplitude corresponding to the minimum Rabi frequency observed in the two configurations. (b) Schematic configurations of UP and DOWN modes for the target qubit Q_{26}. The frequency detunings are set to $\Delta_{\mathrm{NN}}/2\pi$ = 80 MHz, $\Delta_{\mathrm{NNN}}/2\pi$ = 20 MHz, and $\Delta_{\mathrm{rest}}/2\pi$ = 10 MHz, respectively. In the UP mode, all (surrounding) qubits are tuned above the resonant frequency, While in the DOWN mode, they are biased below. (c) Qubit spectroscopy near the resonant frequency of 3.520 GHz over a 100 MHz range, corresponding to the maximum disorder strength. The dashed black line represents the fit using a cubic polynomial function, detail of which is shown in the inset.

2. *Single-qubit population for 21-qubit block segment of multi-qubit on-resonant experiment*

In the Methods, we compare the imbalances between experiment and numerical simulation (see Extended Data Fig.1.). Here, we present a detailed comparison of the single-qubit populations for one of the 21-qubit blocks, shown in Fig.S12. The experimental results show excellent agreement with exact simulations, confirming that both on-resonance qubit biases and coupling strengths in our system are accurately calibrated to their true values.

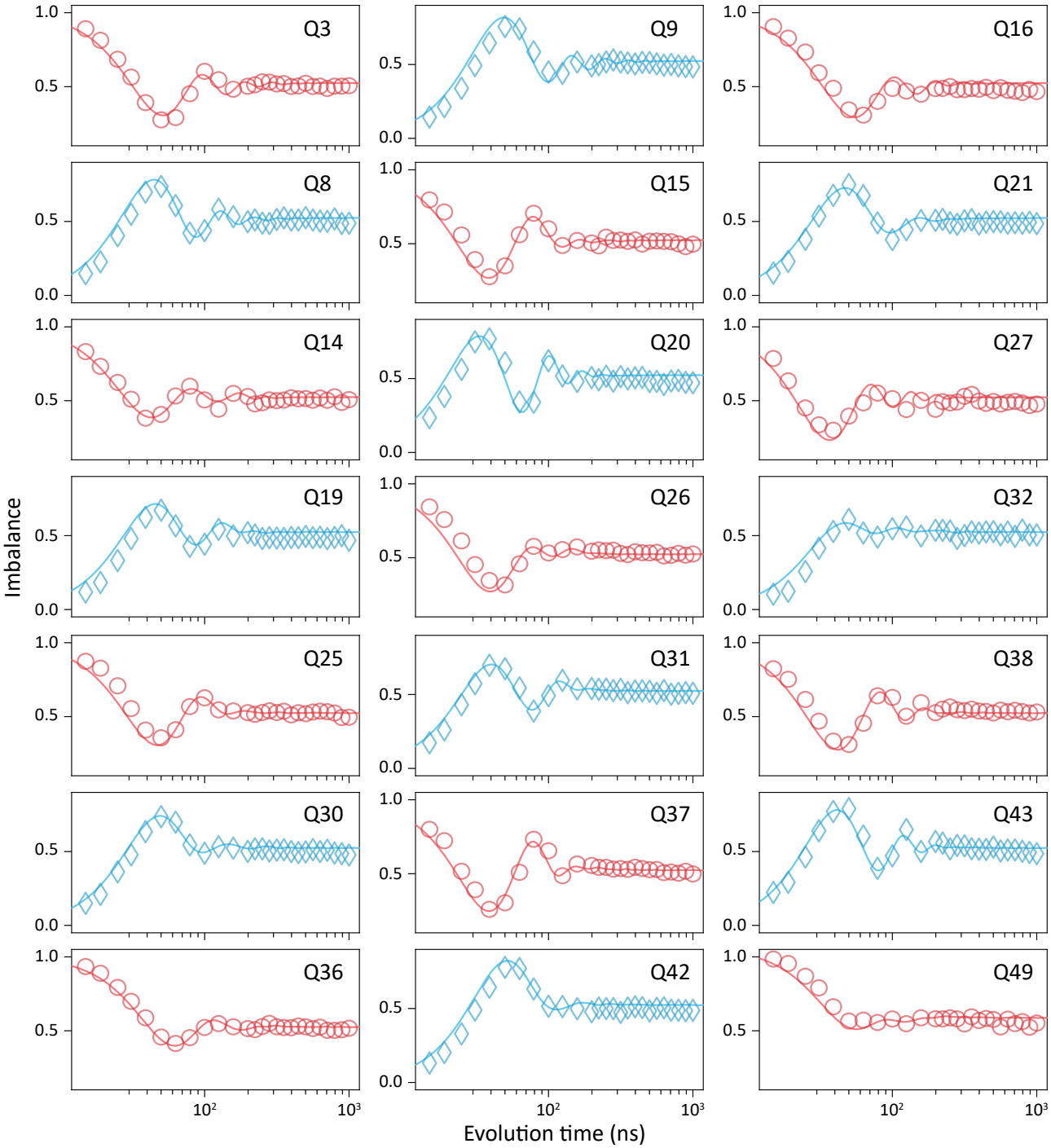

FIG. S12. **Detailed comparison of single-qubit population dynamics in a 21-qubit block.** Experimental measurements (diamonds) and numerical simulations (solid lines) are shown for qubits initialized in $|1\rangle$ (red) and those remaining in $|0\rangle$ (blue). The experimental data closely match the theoretical predictions.

Section 3. SUPPLEMENTARY DATA

A. Dynamics of imbalance for different disorder strengths and system sizes

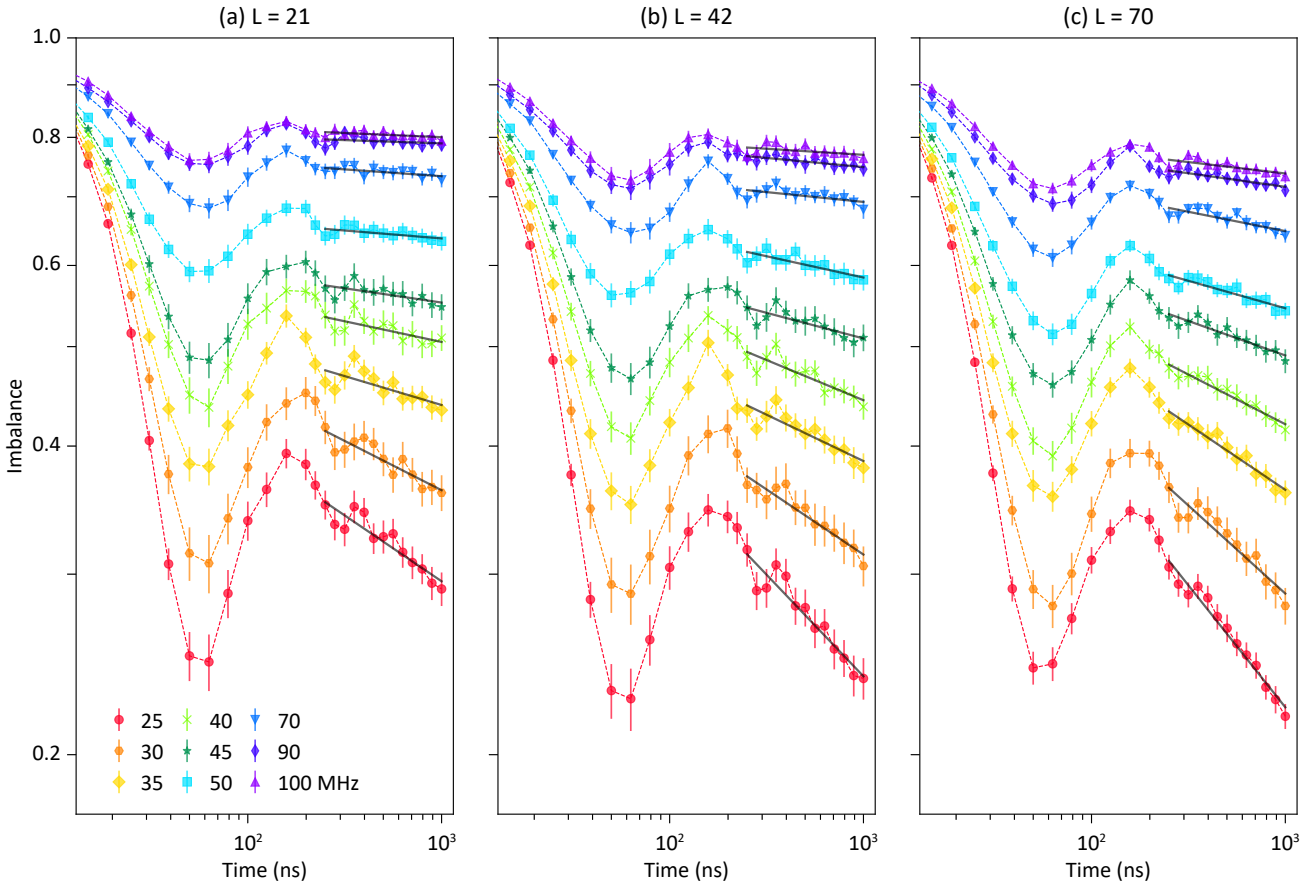

FIG. S13. **Dynamics of imbalance of disordered 2D systems.** Experimental evolution of imbalance under varying disorder strengths (each shown with distinct colors and markers in the legend) for system sizes (a) $L = 21$, (b) $L = 42$ and (c) $L = 70$. Solid black lines depict linear fits used to extract relaxation exponents β. Error bars represent the standard error of the statistical mean calculated over 30 disorder realizations for (a) $n = 10$ and $n = 11$ (60 realizations in total), (b) $n = 21$, (c) $n = 35$.

B. Exponential fitting of experimental relaxation exponents

To characterize how the relaxation exponent β depends on disorder strength W, we examine two models, power-law ($\beta = CW^{-\gamma}$) and exponential ($\beta = Ce^{-\gamma W}$) fitting. Both models can be linearized into functions $\ln(\beta) = -\gamma \ln(W) + \ln(C)$ and $\ln(\beta) = -\gamma W + \ln(C)$. The power-law fit is presented in Fig.3**a** of the main text, while the exponential fit is shown in Fig.S14. In the inset of Fig.S14, the coefficients of determination R^2 are compared: the power-law form yields mean $R^2 = 0.97$, whereas the exponential form gives mean $R^2 = 0.53$. This clear contrast confirms that the power-law relation provides a significantly better description of the experimental data.

C. Numerical data for 1D disordered systems

In the Methods, we briefly introduce the numerical methods adopted in this work, including the polynomially filtered exact diagonalization method (POLFED) for calculating the mean level spacing $\langle r \rangle$, the Krylov subspace method for numerically simulating the quench dynamics for the systems with size $L = 21$, and the time dependent variational principle (TDVP) algorithm

based on the matrix product state (MPS) for simulating the dynamics for the system with size $L = 42$.

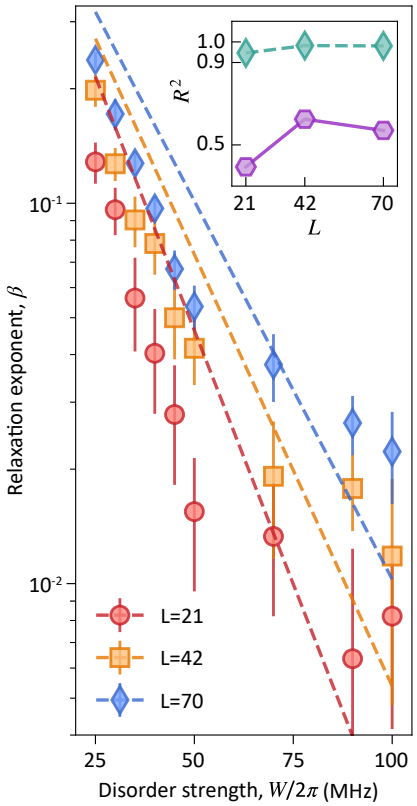

FIG. S14. **Exponential fitting of relaxation exponent β.** The relaxation exponent β is shown against disorder strength W for 2D systems of various sizes L. The dashed lines represent the fittings of β by considering the function $\beta = Ce^{-\gamma W}$ with two fitting parameters C and γ. The inset compares the coefficient of determination R^2 for the linearity between the power-law $\ln(\beta) = -\gamma \ln(W) + \ln(C)$ and exponential $\ln(\beta) = -\gamma W + \ln(C)$ fits.

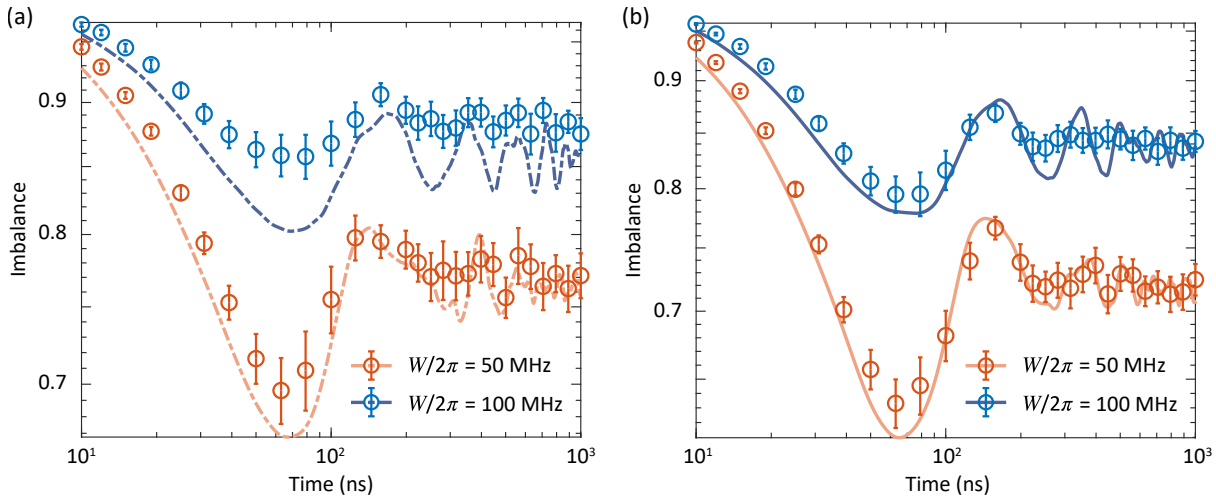

FIG. S15. **Numerical data for disordered 1D systems.** (a) Numerical data for the dynamics of imbalance of 1D disordered systems with different disorder strengths W and the system size $L = 21$, in comparison with the experimental data. (b) is similar to (a) but with a larger system size $L = 42$. The lines and circles represent the numerical and experimental data, respectively.

To benchmark the experimental data for 1D disordered systems (shown in the inset of Fig.2**b** and **c** in the main text), here we also numerically simulate the dynamics of imbalance $I(t)$ for the 1D systems with sizes $L = 21$ and 42. For $L = 21$, we adopt the Krylov subspace method. For $L = 42$, we employ the TDVP algorithm based on MPS with a bond dimension $\chi = 128$. In Fig.S15 (a) and (b), we plot the numerical results of imbalance $I(t)$ for the time evolution of 1D disordered systems with different disorder strengths W and the system size $L = 21$ and 42, respectively. We show that the experimental data are well consistent with the numerical results.

[1] D. T. Sank, *Fast, Accurate State Measurement in Superconducting Qubits*, Ph.D. thesis, University of California, Santa Barbara (2014).

[2] F. Arute, K. Arya, R. Babbush, D. Bacon, J. C. Bardin, R. Barends, R. Biswas, S. Boixo, F. G. S. L. Brandao, D. A. Buell, B. Burkett, Y. Chen, Z. Chen, B. Chiaro, R. Collins, W. Courtney, A. Dunsworth, E. Farhi, B. Foxen, A. Fowler, C. Gidney, M. Giustina, R. Graff, K. Guerin, S. Habegger, M. P. Harrigan, M. J. Hartmann, A. Ho, M. Hoffmann, T. Huang, T. S. Humble, S. V. Isakov, E. Jeffrey, Z. Jiang, D. Kafri, K. Kechedzhi, J. Kelly, P. V. Klimov, S. Knysh, A. Korotkov, F. Kostritsa, D. Landhuis, M. Lindmark, E. Lucero, D. Lyakh, S. Mandrà, J. R. McClean, M. McEwen, A. Megrant, X. Mi, K. Michielsen, M. Mohseni, J. Mutus, O. Naaman, M. Neeley, C. Neill, M. Y. Niu, E. Ostby, A. Petukhov, J. C. Platt, C. Quintana, E. G. Rieffel, P. Roushan, N. C. Rubin, D. Sank, K. J. Satzinger, V. Smelyanskiy, K. J. Sung, M. D. Trevithick, A. Vainsencher, B. Villalonga, T. White, Z. J. Yao, P. Yeh, A. Zalcman, H. Neven, and J. M. Martinis, Quantum supremacy using a programmable superconducting processor, Nature **574**, 505 (2019).

[3] F. Yan, P. Krantz, Y. Sung, M. Kjaergaard, D. L. Campbell, T. P. Orlando, S. Gustavsson, and W. D. Oliver, Tunable coupling scheme for implementing high-fidelity two-qubit gates, Physical Review Applied **10**, 054062 (2018).

[4] Y.-H. Shi, R.-Q. Yang, Z. Xiang, Z.-Y. Ge, H. Li, Y.-Y. Wang, K. Huang, Y. Tian, X. Song, D. Zheng, K. Xu, R.-G. Cai, and H. Fan, Quantum simulation of hawking radiation and curved spacetime with a superconducting on-chip black hole, Nature Communications **14**, 3263 (2023).

[5] E. A. Sete, A. Q. Chen, R. Manenti, S. Kulshreshtha, and S. Poletto, Floating Tunable Coupler for Scalable Quantum Computing Architectures, Physical Review Applied **15**, 064063 (2021).

[6] L. S. Bishop, E. Ginossar, and S. M. Girvin, Response of the strongly driven jaynes-cummings oscillator, Physical Review Letters **105**, 100505 (2010).

[7] M. Boissonneault, J. M. Gambetta, and A. Blais, Improved superconducting qubit readout by qubit-induced nonlinearities, Physical Review Letters **105**, 100504 (2010).

[8] Z. Yan, Y.-R. Zhang, M. Gong, Y. Wu, Y. Zheng, S. Li, C. Wang, F. Liang, J. Lin, Y. Xu, C. Guo, L. Sun, C.-Z. Peng, K. Xia, H. Deng, H. Rong, J. Q. You, F. Nori, H. Fan, X. Zhu, and J.-W. Pan, Strongly correlated quantum walks with a 12-qubit superconducting processor, Science **364**, 753 (2019).

[9] T.-M. Li, J.-C. Zhang, B.-J. Chen, K. Huang, H.-T. Liu, Y.-X. Xiao, C.-L. Deng, G.-H. Liang, C.-T. Chen, Y. Liu, H. Li, Z.-T. Bao, K. Zhao, Y. Xu, L. Li, Y. He, Z.-H. Liu, Y.-H. Yu, S.-Y. Zhou, Y.-J. Liu, X. Song, D. Zheng, Z. Xiang, Y.-H. Shi, K. Xu, and H. Fan, High-precision pulse calibration of tunable couplers for high-fidelity two-qubit gates in superconducting quantum processors, Physical Review Applied **23**, 024059 (2025).

[10] F. Motzoi, J. M. Gambetta, P. Rebentrost, and F. K. Wilhelm, Simple pulses for elimination of leakage in weakly nonlinear qubits, Physical Review Letters **103**, 110501 (2009).

[11] S. Xu, Z.-Z. Sun, K. Wang, L. Xiang, Z. Bao, Z. Zhu, F. Shen, Z. Song, P. Zhang, W. Ren, X. Zhang, H. Dong, J. Deng, J. Chen, Y. Wu, Z. Tan, Y. Gao, F. Jin, X. Zhu, C. Zhang, N. Wang, Y. Zou, J. Zhong, A. Zhang, W. Li, W. Jiang, L.-W. Yu, Y. Yao, Z. Wang, H. Li, Q. Guo, C. Song, H. Wang, and D.-L. Deng, Digital simulation of projective non-abelian anyons with 68 superconducting qubits, Chinese Physics Letters **40**, 060301 (2023).

[12] Y.-Y. Wang, Y.-H. Shi, Z.-H. Sun, C.-T. Chen, Z.-A. Wang, K. Zhao, H.-T. Liu, W.-G. Ma, Z. Wang, H. Li, J.-C. Zhang, Y. Liu, C.-L. Deng, T.-M. Li, Y. He, Z.-H. Liu, Z.-Y. Peng, X. Song, G. Xue, H. Yu, K. Huang, Z. Xiang, D. Zheng, K. Xu, and H. Fan, Exploring hilbert-space fragmentation on a superconducting processor, PRX Quantum **6**, 010325 (2025).

[13] T. I. Andersen, N. Astrakhantsev, A. H. Karamlou, J. Berndtsson, J. Motruk, A. Szasz, J. A. Gross, A. Schuckert, T. Westerhout, Y. Zhang, E. Forati, D. Rossi, B. Kobrin, A. D. Paolo, A. R. Klots, I. Drozdov, V. Kurilovich, A. Petukhov, L. B. Ioffe, A. Elben, A. Rath, V. Vitale, B. Vermersch, R. Acharya, L. A. Beni, K. Anderson, M. Ansmann, F. Arute, K. Arya, A. Asfaw, J. Atalaya, B. Ballard, J. C. Bardin, A. Bengtsson, A. Bilmes, G. Bortoli, A. Bourassa, J. Bovaird, L. Brill, M. Broughton, D. A. Browne, B. Buchea, B. B. Buckley, D. A. Buell, T. Burger, B. Burkett, N. Bushnell, A. Cabrera, J. Campero, H. S. Chang, Z. Chen, B. Chiaro, J. Claes, A. Y. Cleland, J. Cogan, R. Collins, P. Conner, W. Courtney, A. L. Crook, S. Das, D. M. Debroy, L. D. Lorenzo, A. D. T. Barba, S. Demura, P. Donohoe, A. Dunsworth, C. Earle, A. Eickbusch, A. M. Elbag, M. Elzouka, C. Erickson, L. Faoro, R. Fatemi, V. S. Ferreira, L. F. Burgos, A. G. Fowler, B. Foxen, S. Ganjam, R. Gasca, W. Giang, C. Gidney, D. Gilboa, M. Giustina, R. Gosula, A. G. Dau, D. Graumann, A. Greene, S. Habegger, M. C. Hamilton, M. Hansen, M. P. Harrigan, S. D. Harrington, S. Heslin, P. Heu, G. Hill, M. R. Hoffmann, H. Y. Huang, T. Huang, A. Huff, W. J. Huggins, S. V. Isakov, E. Jeffrey, Z. Jiang, C. Jones, S. Jordan, C. Joshi, P. Juhas, D. Kafri, H. Kang, K. Kechedzhi, T. Khaire, T. Khattar, M. Khezri, M. Kieferová, S. Kim, A. Kitaev, P. Klimov, A. N. Korotkov, F. Kostritsa, J. M. Kreikebaum, D. Landhuis, B. W. Langley, P. Laptev, K. M. Lau, L. L. Guevel, J. Ledford, J. Lee, K. W. Lee, Y. D. Lensky, B. J. Lester, W. Y. Li, A. T. Lill, W. Liu, W. P. Livingston, A. Locharla, D. Lundahl, A. Lunt, S. Madhuk, A. Maloney, S. Mandrà, L. S. Martin, O. Martin, S. Martin, C. Maxfield, J. R. McClean, M. McEwen, S. Meeks, K. C. Miao, A. Mieszala, S. Molina, S. Montazeri, A. Morvan, R. Movassagh, C. Neill, A. Nersisyan, M. Newman, A. Nguyen, M. Nguyen, C. H. Ni, M. Y. Niu, W. D. Oliver, K. Ottosson, A. Pizzuto, R. Potter, O. Pritchard, L. P. Pryadko, C. Quintana, M. J. Reagor, D. M. Rhodes, G. Roberts, C. Rocque, E. Rosenberg, N. C. Rubin, N. Saei, K. Sankaragomathi, K. J. Satzinger, H. F. Schurkus, C. Schuster, M. J. Shearn, A. Shorter, N. Shutty, V. Shvarts, V. Sivak,

J. Skruzny, S. Small, W. C. Smith, S. Springer, G. Sterling, J. Suchard, M. Szalay, A. Sztein, D. Thor, A. Torres, M. M. Torunbalci, A. Vaishnav, S. Vdovichev, B. Villalonga, C. V. Heidweiller, S. Waltman, S. X. Wang, T. White, K. Wong, B. W. K. Woo, C. Xing, Z. J. Yao, P. Yeh, B. Ying, J. Yoo, N. Yosri, G. Young, A. Zalcman, N. Zhu, N. Zobrist, H. Neven, R. Babbush, S. Boixo, J. Hilton, E. Lucero, A. Megrant, J. Kelly, Y. Chen, V. Smelyanskiy, G. Vidal, P. Roushan, A. M. Läuchli, D. A. Abanin, and X. Mi, Thermalization and criticality on an analogue–digital quantum simulator, Nature **638**, 79 (2025).